

Superelasticity and functional fatigue of single crystalline FeNiCoAlTi iron-based shape memory alloy

Wael Abuzaid^{a,b,*}, Huseyin Sehitoglu^c

^a Department of Mechanical Engineering, American University of Sharjah, PO Box 26666, Sharjah, United Arab Emirates

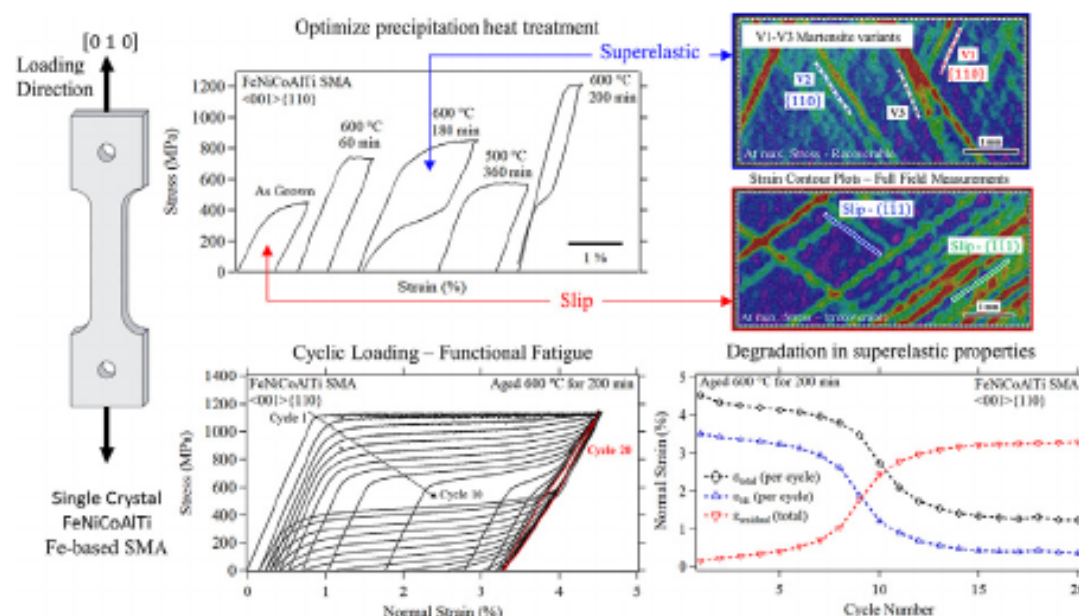
^b Materials Science and Engineering Research Institute, American University of Sharjah, PO Box 26666, Sharjah, United Arab Emirates

^c Department of Mechanical Science and Engineering, University of Illinois at Urbana-Champaign, 1206 W. Green St., Urbana, IL 61801, USA

HIGHLIGHTS

- FeNiCoAlTi iron-based shape memory alloy was investigated following various heat treatments and loading conditions
- Local accumulation of irrecoverable strains was measured despite high recovery rates based on global strain measurements
- Under cyclic loading conditions, loss of superelasticity was limited initially but became significant after 10 cycles
- Functionality loss was attributed to the buildup of local irrecoverable strains and plasticity at the martensite boundary

GRAPHICAL ABSTRACT



ARTICLE INFO

Article history:

Received 3 August 2018

Received in revised form 28 September 2018

Accepted 2 October 2018

Available online 03 October 2018

Keywords:

Iron-based shape memory alloy

FeNiCoAlTi

Single crystal

Superelasticity

Functional fatigue

Irrecoverable strains

ABSTRACT

The development of Iron-based shape memory alloys is primarily motivated by the need for a cost-effective alternative to NiTi. This work explores the superelastic and functional fatigue properties of Fe_{42.5}Ni₃₀Co₁₅Al₁₀Ti_{2.5} SMA. Single crystalline samples were subjected to various heat treatments to optimize the precipitation content and achieve superelastic response. Precipitation heat treatments between 180 and 200 min at 600 °C were conducive to superelasticity with large recoverable strains (~7%) and high levels of recovery (>95% recovery). Heat treatments at lower temperatures altered the strength but without achieving superelasticity. A phenomenon which was attributed to plastic slip resulting from the critical transformation stress being higher than the slip resistance. Treatment times beyond 200 min induced a brittle response and premature fracture prior to transformation. Cyclic experiments were also conducted following different heat treatments and loading conditions to study the functional fatigue properties. In all cases, limited degradation of superelastic properties took place in the first 10 cycles. However, with continued loading, reduction of superelastic strains and loss of functionality was observed. This was attributed to the gradual buildup of local irrecoverable strains due to plasticity at the martensite boundary which acts to pin the interface and prevent reverse transformation.

© 2018 Elsevier Ltd. All rights reserved.

1. Introduction

Research focused on the development and characterization of shape memory alloys (SMA) has enabled advanced applications utilizing their unique shape memory (SM) and superelastic (SE) properties [1–10].

* Corresponding author at: Department of Mechanical Engineering, American University of Sharjah, PO Box 26666, Sharjah, United Arab Emirates.

E-mail address: wabuzaid@aus.edu (W. Abuzaid).

The widely studied, and commercially available, NiTi based compositions continue to be the materials of choice in the development of practical applications due to their large transformation strains, high slip resistance, and good functional properties under cyclic loading conditions [11–14]. However, the cost associated with manufacturing NiTi and the high sensitivity to composition variation prevents a wider adoption and use of this class of shape memory materials in structural applications. The development of Fe-based, or ferrous SMAs, has been motivated by the need for a cost-effective SMA with more commercially attractive processing routes [3,15,16]. Various alloys have been proposed such as the FeNi, FeMn, FeMnSi, FeNiCoTi, FePd and FePt based compositions [1,17]. However, obtaining the desirable room temperature superelasticity has been a challenge in the aforementioned Fe-based SMAs. Recent efforts focused on FeNiCoAlX (where X is either Ta or Ti) and FeMnAlNi compositions are of particular interest and several studies have reported large superelastic and recoverable strains at room temperature [18–22]. A major drawback, however, is the degradation of superelastic properties under cyclic loading condition (*i.e.*, functional fatigue) [16,23]. A phenomenon that has been primarily attributed to pinning of the martensite interface boundary which prevents complete reversibility and results in the accumulation of residual strains with continued loading [16]. The rate of degradation in SE properties and the accumulation of residual strains are influenced by the loading level (*i.e.*, total applied cyclic strain) and aging heat treatment. This work is focused on studying the functional fatigue properties of single crystalline Fe_{42.5}Ni₃₀Co₁₅Al₁₀Ti_{2.5} (at.%) Fe-based SMA. Through the use of local and full-field deformation measurements, the work provides a quantitative assessment and further insight into the degradation of superelastic strains for samples subjected to different heat treatments and cyclic loading conditions.

The FeNiCoAlTa Fe-based SMA, first reported by Tanaka et al., undergoes a reversible fcc (austenite) to bct (martensite) stress-induced phase transformation [21]. With proper control of texture (*i.e.*, $\langle 100 \rangle$ textured polycrystalline) and aging treatment, large critical transformation stresses (>1000 MPa) and large transformation strains on the order of 13% were reported. Aging heat treatments are typically required in this class of alloy, and in Fe-based SMAs in general, to introduce γ' precipitates which are essential for inducing reversible martensitic transformation, and therefore superelasticity [19,22,24–28]. In the case of FeNiCoAlTi, the aging treatments introduce ordered L1₂ γ' precipitates (5–10 nm diameter) and (FeNiCo)₃(AlTi) chemical composition into the austenite matrix [29]. As the aging treatment and the resultant precipitation process is time and temperature dependent, a proper optimization of the heat treatment parameters is essential to prevent excessive precipitation (note that the precipitates do not undergo transformation) or the formation of large precipitates which would degrade ductility and induce a brittle response. Previous work considering FeNiCoAlX (where X = Ta or Ti) have reported reversible martensitic transformation and superelastic properties with aging treatments conducted at temperatures ranging from 600 to 700 °C. The aging duration varies significantly between the two compositions (*i.e.*, alloying FeNiCoAl with Ta or Ti) with the lighter Ti atoms allowing for shorter aging times (1–4 h) compared to the heavier Ta (up to 90 h) [24,25,30]. This particular aspect has sparked additional interest in the FeNiCoAlTi based SMA. Although several studies have reported extensive experimental analysis of the superelastic properties of FeMnCoAlTi SMA, including works considering single crystals [25,29,31], quantitative assessment of the functional fatigue properties under cyclic loading remains limited. This particular aspect will be a subject of investigation in this work utilizing Fe_{42.5}Ni₃₀Co₁₅Al₁₀Ti_{2.5} (at.%) single crystals. The selection of single crystal samples, as opposed to polycrystalline, is primarily motivated by the tendency of the polycrystalline material to develop precipitates at grain boundaries thus limiting superelasticity and causing an undesirable

crystal orientation was selected, the $\langle 001 \rangle$, which has the largest magnitude of strain recovery based on theoretical calculations.

Different aspects control the SE response in Fe-based SMAs including the material phase prior to loading (should be austenite), the dispersion of γ' precipitates, and the austenite resistance to slip [32]. Unlike NiTi, the separate assessment of all of these contributing factors is challenging in Fe-based SMAs. For example, differential scanning calorimetry (DSC) can be easily used to determine the transformation temperature in NiTi. Such measurements in Fe-based SMAs are not possible and researchers resort to different approaches such as resistivity or magnetization measurements [21,24]. Isobaric (*i.e.*, constant stress loading with temperature cycling) have also been used, however, the results are stress dependent [29,33–35]. The dynamic mechanical analyzer (DMA) enables similar measurements by capturing the change in material stiffness following phase transformation. Multiple studies have utilized the DMA to evaluate the shape memory properties and phase transformation temperatures in NiTi, including comparison with DSC results [36–38]. As for the γ' nano-scale precipitates, its well documented that their presence is essential to obtain a thermo-elastic martensitic transformation (*i.e.*, superelasticity). The hardening induced by the presence of these precipitates affects not only the austenite slip resistance but can also, as will be shown in this work, alter the critical martensitic transformation stress. Therefore, a proper assessment and control of the amount of dispersion and size of the γ' precipitates is of great importance, however, requires extensive analysis using techniques such as TEM and tomography [24,33]. The collective impact of all of these contributing factors is typically captured at the macro-scale in the form of a stress-strain curve. In the case that no superelasticity is observed, assessing the cause becomes a formidable task based on macro-scale measurements only. The use of local and full-field strain measurements provides additional insight into the problem and can guide optimization efforts. For example, plastic deformation in the austenite phase and non-reversible martensitic phase transformation will have similar macro-scale response (*i.e.*, stress-strain curves), however, the local strain fields will differ significantly. In this work, full-field measurements using digital image correlation (DIC) were utilized to unambiguously differentiate between plastic slip dominated deformation and phase transformation. By locally assessing the plastic strain field, the lack of superelasticity for some samples was attributed to improper aging treatment resulting in slip resistance that is lower than the critical transformation stress. The approach has helped explain the lack of superelasticity in the macro-scale measurements and has facilitated optimizing the aging treatment conditions to obtain the desirable room temperature superelasticity.

In summary, the superelastic deformation response of single crystalline FeNiCoAlTi Fe-based SMA was investigated in this study under different loading conditions with focus on the functional fatigue properties. The $\langle 001 \rangle$ orientation was selected as it provides the largest magnitude of theoretical transformation strains (8.7% in tension) [21]. Samples were subjected to various aging heat treatment to optimize the room temperature superelastic strains. Through the use of local and full-field deformation measurements, the lack of superelasticity for some heat treatments was explained based on the difference in the local deformation fields for samples undergoing reversible phase transformation and samples exhibiting no SE strain recovery. We finally provide quantitative insight into the functional fatigue properties for samples subjected to different levels of deformation (3% and 4.5% total cyclic strain) and different aging treatments (600 °C for 180 min and 200 min). In particular, the rate of degradation in SE strains and the accumulation of residual strains were evaluated under cyclic loading conditions.

2. Materials and methods

subjected to a 33 h homogenization heat treatment at 1285 °C prior to cutting samples using electric discharge machining. Dogbone tensile samples with 1.5 mm × 3 mm gauge section were machined with the loading axis aligned with the ⟨001⟩ crystallographic direction. Samples were subjected to various aging heat treatments at temperatures ranging from 500 to 600 °C. All treatments were conducted in air and terminated with quenching in water. To prepare samples for full-field DIC measurements, the surface of each aged specimen was polished using SiC paper to remove any surface scratches. A fine black paint speckle pattern was applied using an airbrush.

Deformation was performed using an Instron servo-hydraulic load frame with loading conducted in strain control with an average strain rate of 10^{-3} s^{-1} (using a 5 mm gauge length extensometer) and unloading in load control. For samples deformed at room temperature (RT), DIC reference and deformed images were captured covering approximately a 5 mm × 3 mm region of interest with an imaging resolution of (~4 μm/pixel). During deformation (loading and unloading), optical images were captured every 2 s. As explained in the introduction, the focus of this study is on the superelastic response of the single crystalline Fe-based SMA FeNiCoAlTi. A schematic detailing all the experimental parameters which describe the SMA superelastic response is presented in Fig. 1. The stress points σ_f and σ_r point to the critical forward and reverse transformation stresses, respectively. The total applied strain during loading (ϵ_{total}) is broken down into a recoverable ($\epsilon_{\text{recoverable}}$) and irrecoverable or residual strain ($\epsilon_{\text{residual}}$) components. The total strain recovery includes the superelastic strain (ϵ_{SE}) and the recoverable elastic strains.

3. Results and analysis

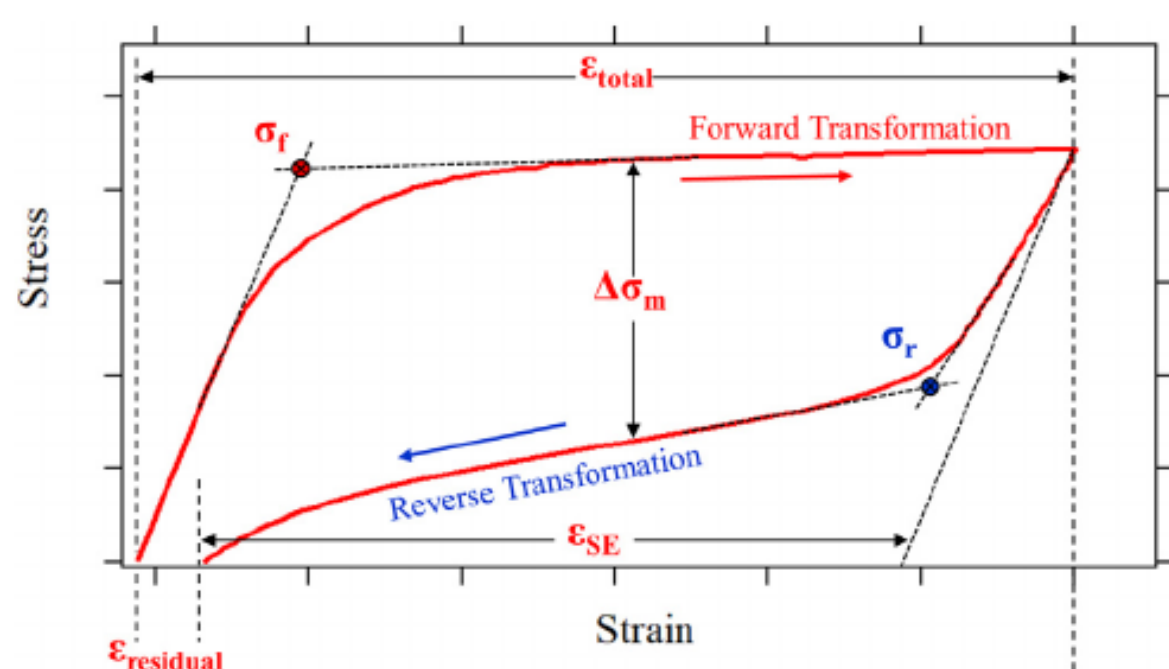
Fig. 2a shows the stress-strain response for different single crystalline samples subjected to various aging heat treatments. The loading direction for all the specimens was along the ⟨100⟩ crystallographic direction which, as explained in the introduction, has the largest magnitude of theoretical transformation strains. After 60 min of aging treatment at 600 °C, the stress level as observed from the stress-strain curve has increased from around 400 MPa for the as-grown conditions (i.e., homogenized and without any aging treatment) to ~800 MPa. The stress increase is associated with the anticipated, and desired precipitation process, however, no superelasticity was detected. By increasing the aging treatment time from 60 min to 180 min, the strength increased further and a clear superelastic response was observed. At 200 min aging time (only 20 min increase), further amplification in strength was observed and the samples continued to exhibit good SE behavior. Slight modifications to the aging time beyond 200 min caused

very high stress levels and brittle fracture prior to macro-scale plasticity or superelasticity. A similar brittle behavior was also observed for higher temperature aging treatments (i.e., 700 °C – not shown in Fig. 2). Samples subjected to lower temperature aging treatments (e.g., 500 °C as shown in Fig. 2) did not exhibit superelasticity despite the strength increase.

As explained in the introduction, full-field strain measurements using DIC can provide further insight into the local deformation and, therefore, help explain the lack of SE behavior for some samples. A representative contour plot displaying the normal strains (i.e., along the ⟨100⟩ loading direction) for a sample undergoing reversible SE deformation is shown in Fig. 2b. The DIC contour plot captures the activation of 3 different martensite variants (marked as V1, V2, and V3 in Fig. 2b) which is expected for this crystal orientation under tensile loading conditions. The martensitic transformation in this alloy, fcc austenite to bct martensite, follows the Bain cubic to tetragonal deformation and can be accommodated by three martensite variants as described in detail in [18,21]. The twinning plane for such transformation belong to the {110} plane and will, therefore, generate significantly different traces on the sample's surface compared to slip on the {111} planes [26]. For comparison, the contour plot obtained from a non-transforming sample is shown in Fig. 2c. Clearly both contour plots in Fig. 2b and c show a very different local behavior. The strain bands in the non-transforming sample match the traces of the {111} planes (see also Fig. 3). The contour plot shown in Fig. 2c was obtained following a 500 °C aging treatment, however, as-grown samples and the sample aged for 60 min only at 600 °C exhibited a similar response. Since the crystal structure in the austenite phase is fcc, this suggests, based on the local DIC results, that the samples showing no SE strains did not exhibit noticeable martensitic transformation (neither reversible nor non-reversible) and the deformation was dominated by plastic slip on the {111} fcc slip planes. The Schmid factors for the 12 possible fcc slip systems are shown in Fig. 3a. Activation of multiple slip systems is expected with possible traces from all slip planes. Although the exact number of activated slip systems is hard to determine based on such analysis, it is easy to conclude slip mediated plasticity by matching the expected slip plane traces (Fig. 3b) with the strain bands obtained from DIC measurements (Fig. 2c). It is noted that the expected traces for martensitic transformation are of the {110} [24] type which will generate completely different traces on the samples' surface as shown in Fig. 3b and experimentally in Fig. 2b.

Based on the previous results, it is concluded that the deformation in the absence of superelasticity is dominated by plastic slip on the {111} fcc slip planes. The precipitation process induced by aging altered the slip resistance (compare as-grown response to 60 min aging in Fig. 2a) as well as the critical transformation stress (compare 180 min to 200 min aging in Fig. 2a). Therefore, a careful optimization of the aging treatment parameters is required to alter both stresses (i.e., slip resistance and critical transformation stress) such that they are in the correct range where the slip resistance ends up exceeding the transformation stress, thus resulting in SE reversible martensitic transformation.

As reported in Fig. 2, samples subjected to a 180 min aging time exhibited superelasticity at RT. Loading at lower deformation temperatures is expected to display similar SE behavior as long as the deformation temperature is higher than the martensite transformation temperature (M_s). The stress-strain curves presented in Fig. 4a reveal SE strains and high levels of recovery between RT and ~50 °C deformation temperatures. However, once loading was conducted at ~100 °C, a degradation in the SE strains was observed with significant accumulation of



residual deformation. This deformation temperature can potentially be lower than the martensite transformation temperature (M_s) which will therefore adversely affect superelasticity. As discussed in the introduction, DSC measurements, which are predominately used in SMAs, do not typically aid in the determination of phase transformation temperatures in the case of Fe-based SMAs. Therefore, a direct confirmation

Fig. 1. Illustration of the superelastic response in shape memory alloys (deformation at a temperature $>$ austenite finish temperature A_f). The functional degradation in properties is typically manifested as a reduction in the superelastic strains (ϵ_{SE}) and accumulation of residual strains ($\epsilon_{residual}$).

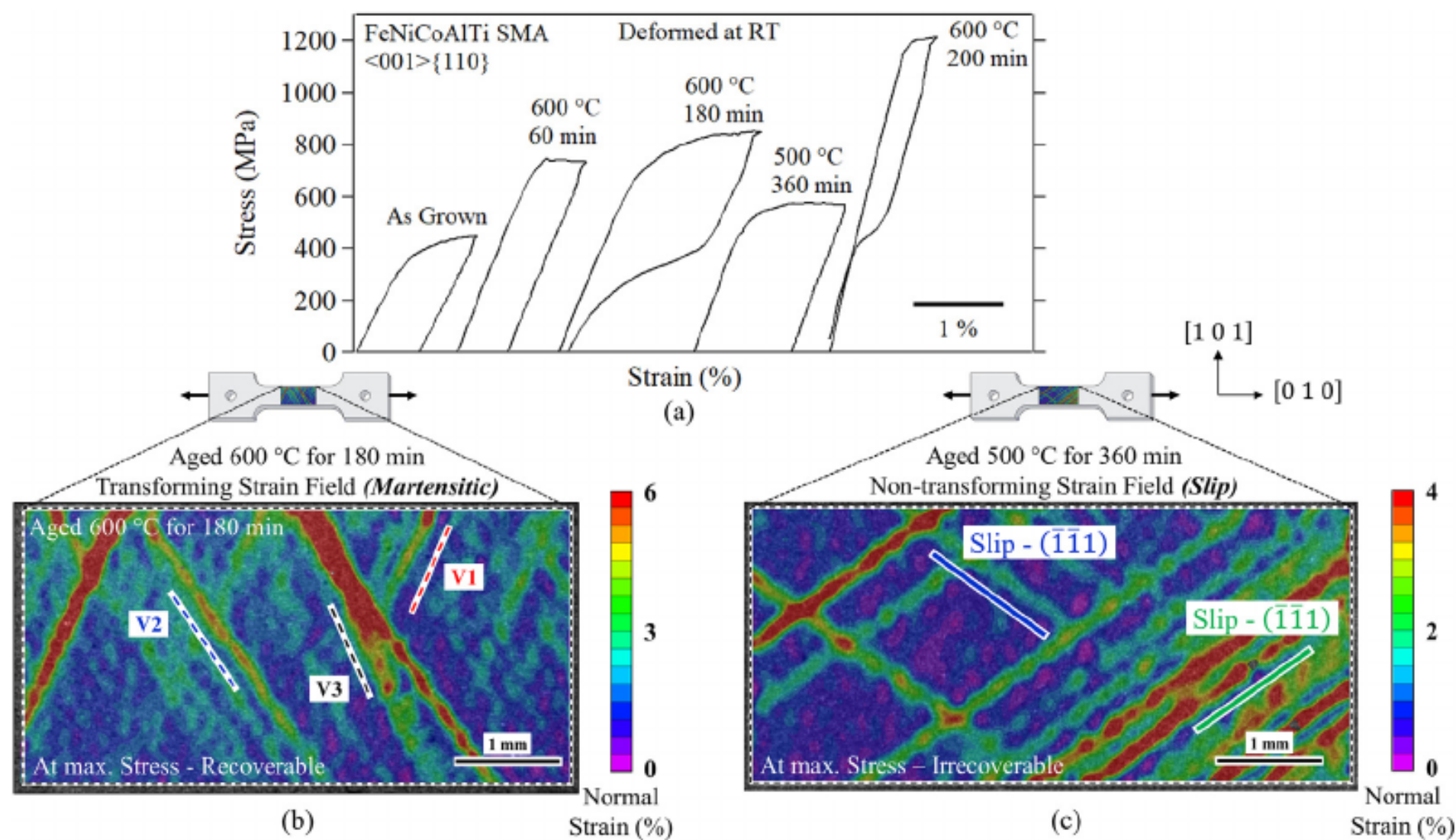


Fig. 2. (a) Stress-strain response of single crystalline FeNiCoAlTi subjected to various aging heat treatments. All samples loaded in tension along the $\langle 100 \rangle$ crystallographic direction. (d) Full-field contour plot showing the normal DIC strains (along the loading direction) for a sample undergoing reversible SE martensitic transformation accommodated by three variants; V1, V2, and V3. (c) Contour plot showing the local strains for a sample exhibiting no SE strains. The non-recoverable strain bands match the traces of the $\{111\}$ fcc slip planes.

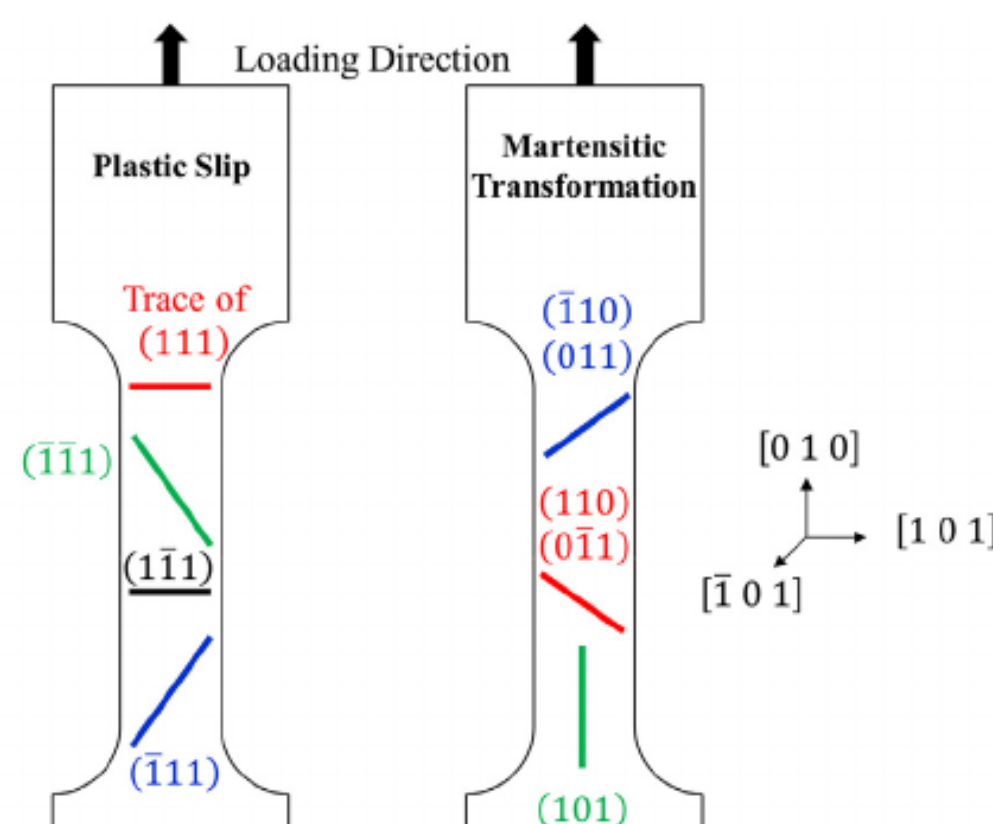
using phase transformation temperatures was not possible. Fig. 4b presents the storage modulus and tan delta which were obtained by conducting a temperature sweep using the DMA on a 180 min aged specimen and as-grown samples. A drop in the storage modulus, and an increase in tan delta, took place around 100 °C which suggests that $M_s \approx 100$ °C. The DMA data provides further evidence that the degradation in SE strains observed at 100 °C was associated with excessive temperature drop inducing the formation of non-transforming, temperature induced, martensite phase.

For samples exhibiting no superelasticity at RT (e.g., following aging for 60 min, which revealed slip dominated plasticity at RT as shown in Fig. 2a), SE response can be induced at lower deformation temperatures

due to the expected drop in the critical transformation stress (σ_f) and increase in the slip resistance with temperature decrease (see Fig. 4d). The stress-strain curves presented in Fig. 4c reveal SE strains starting at 4 °C deformation temperature and down to -100 °C. It is finally worth noting that lowering the deformation temperature, down to -50 °C, for as-grown samples (*i.e.*, no aging treatments) did not cause any superelastic properties and the stress-strain curves exhibited typical plastic response with incremental strength increase with each deformation temperature drop.

For a proper quantitative understanding of the functional fatigue properties of superelastic SMAs, it is important to investigate the *global* as well as the *local* material response. Fig. 5a reports global, and local

Slip System	Schmid Factor
$(111)[\bar{1}01]$	0.00
$(111)[1\bar{1}0]$	0.41
$(111)[0\bar{1}1]$	0.41
$(\bar{1}\bar{1}1)[0\bar{1}\bar{1}]$	0.41
$(\bar{1}\bar{1}1)[\bar{1}0\bar{1}]$	0.00
$(\bar{1}\bar{1}1)[1\bar{1}0]$	0.41
$(1\bar{1}\bar{1})[0\bar{1}\bar{1}]$	0.41
$(1\bar{1}\bar{1})[\bar{1}01]$	0.00
$(1\bar{1}\bar{1})[\bar{1}\bar{1}0]$	0.41
$(\bar{1}11)[\bar{1}0\bar{1}]$	0.00



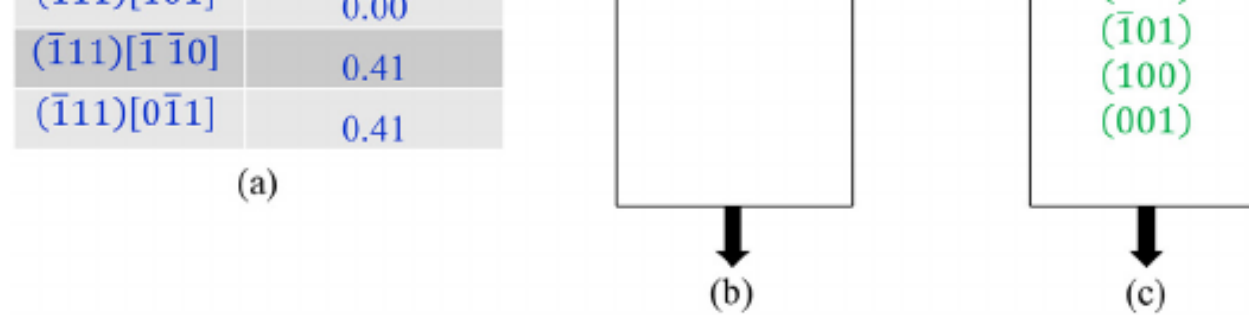


Fig. 3. (a) Schmid factors for the 12 possible slip system in the fcc austenite phase. (b) Possible slip traces of the slip planes {111}. (c) Traces of the {110} planes associated with potential martensite variants.

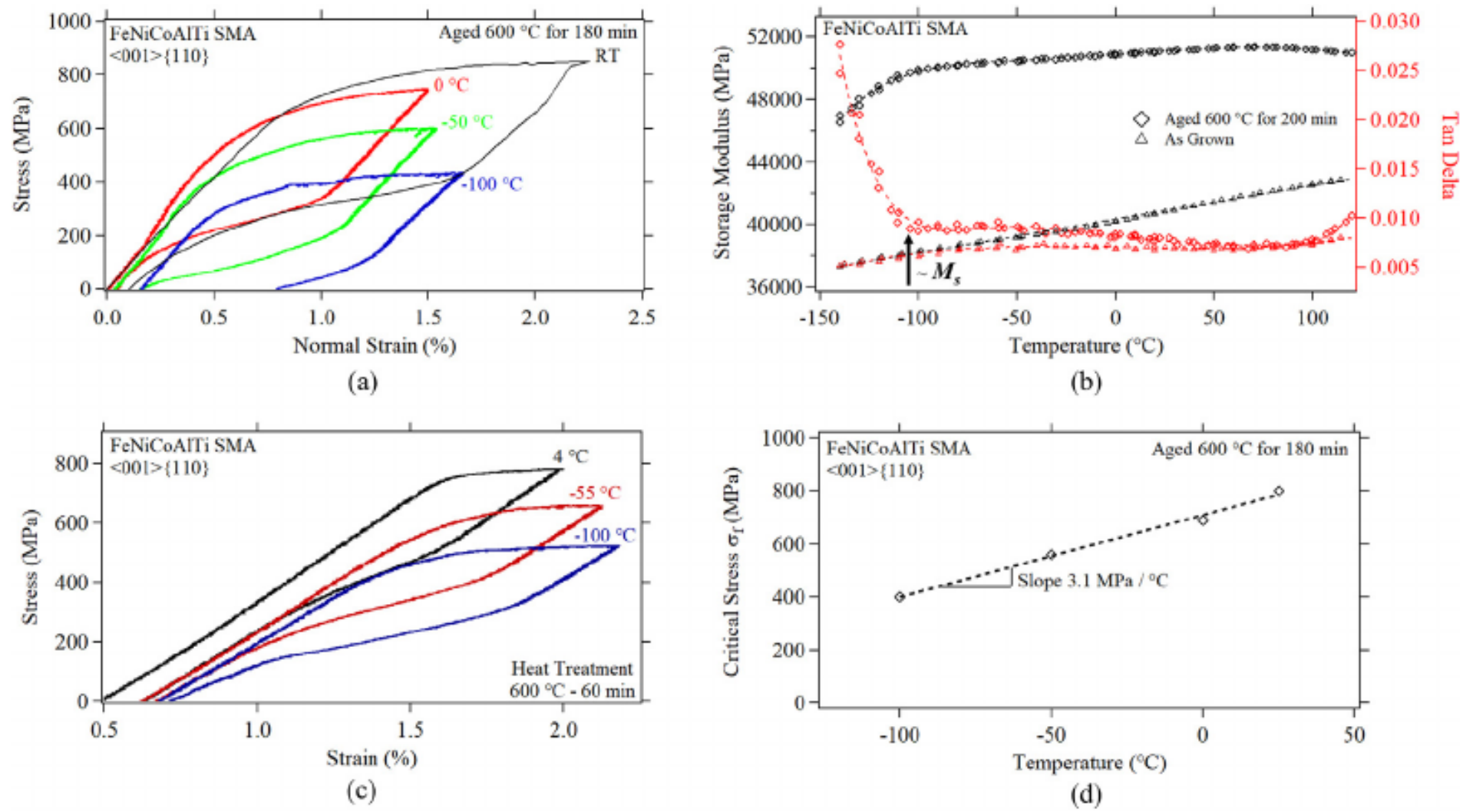
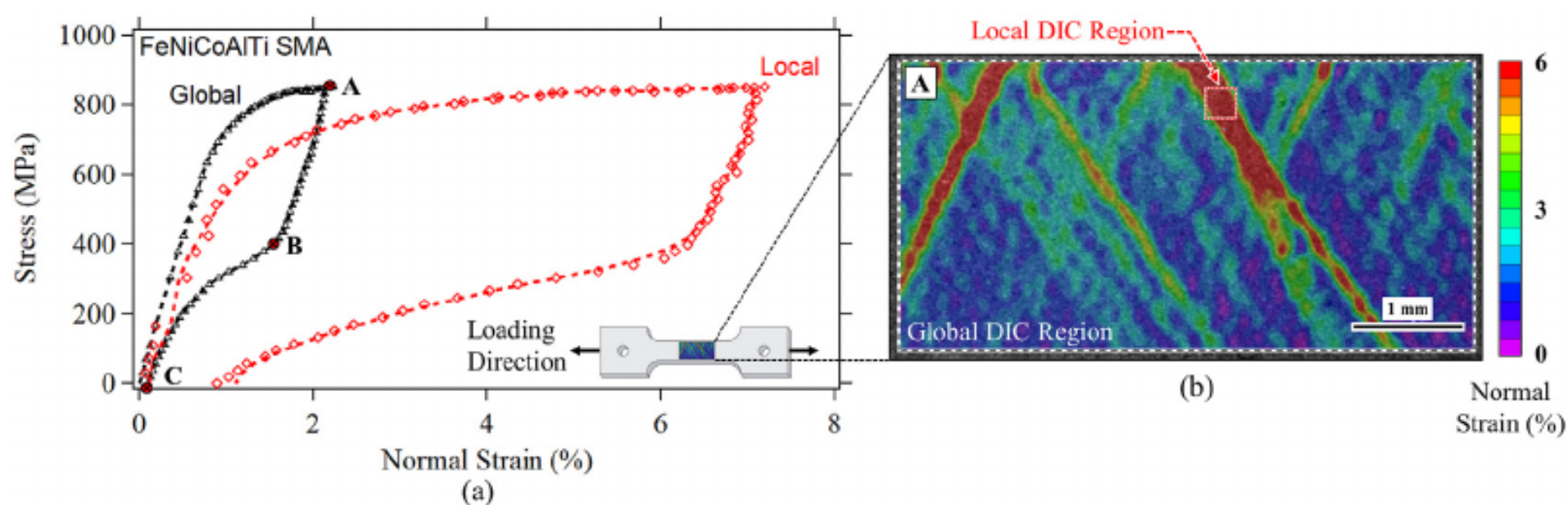


Fig. 4. (a) Stress-strain response at different deformation temperatures for a single crystalline FeNiCoAlTi sample subjected to 180 min aging treatment. (b) The storage modulus and tan delta for as-grown and aged samples. (c) Stress-strain response at different deformation temperatures for a sample subjected to 60 min aging treatment. (d) The critical transformation stress (σ_f) as a function of temperature. Data extracted from (a).

stress-strain curves for a single crystalline FeNiCoAlTi sample exhibiting SE properties. The strains calculated to construct the “Global” curve represent the DIC field averages in the entire region of interest as outlined in Fig. 5b. The “Local” curve was plotted using the localized strains in a small region of interest having the highest strain magnitudes in the DIC field. The global average response, which is equivalent to extensometer measurements, points to full recovery following unloading with no accumulation of residual deformation. However, the local response displayed two notable differences; the magnitude of the local strains exceeded the global average by at least a factor of 3 (reaching 7% locally for 2% applied average strain), and a finite accumulation of residual and

irrecoverable strains was detected. This observation of local accumulation of residual strains can also be visualized using the full-field contour plot of the normal DIC strains (*i.e.*, along the loading direction) following complete unloading as shown in Fig. 5d. It is important to emphasize that despite the seemingly complete recovery from the global measurements, at the macro-scale, local accumulation of residual strains took place.

As discussed previously, the aging treatment had a significant impact on both; the austenite slip resistance and the critical forward transformation stress. The desirable superelastic behavior was only achieved in two of the considered aging treatments, namely the 180 min and



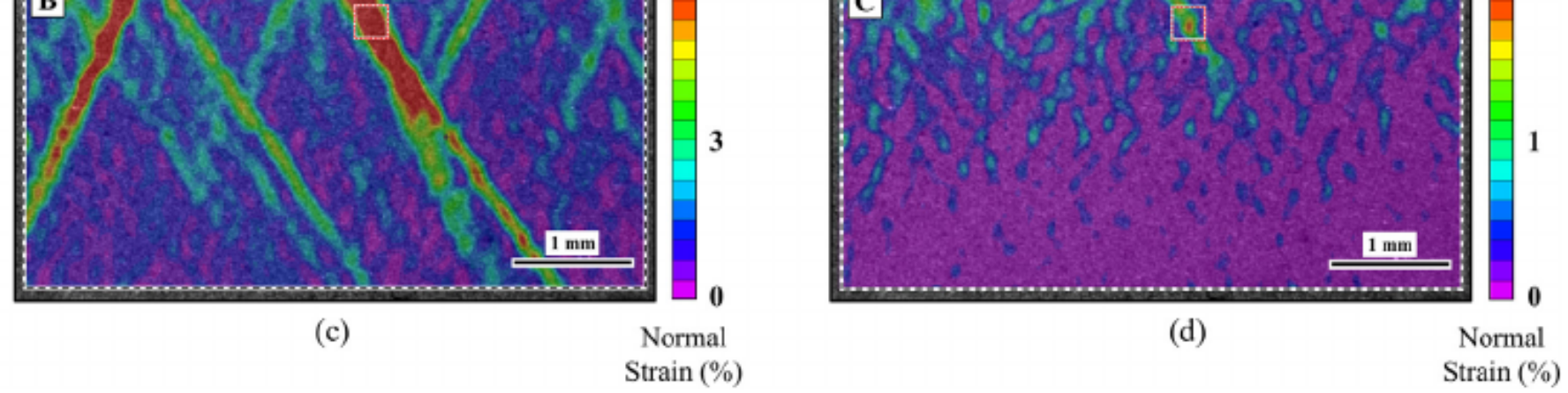


Fig. 5. (a) Global and local stress-strain curves of a single crystalline sample exhibiting superelastic response. (b) Full-field contour plot of the normal strains captured at the maximum stress, point A as marked in (a). The global as well as the local DIC regions used to calculate the strains plotted in (a) are marked with black and red rectangles, respectively. (c)–(d) Full-field contour plot of the normal strains at the onset of reversed transformation, point B which is captured at ϵ_r , and after unloading, respectively.

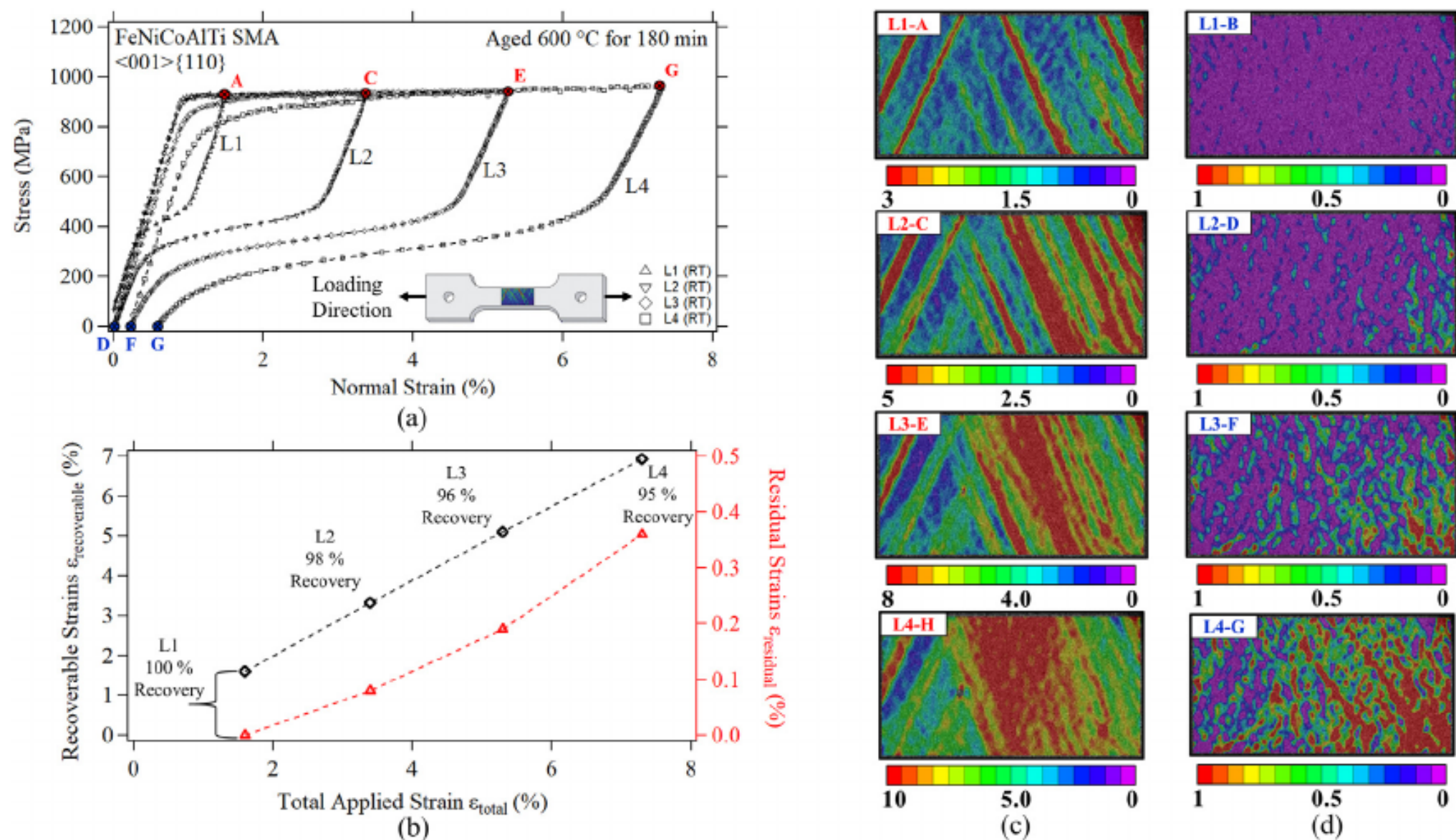
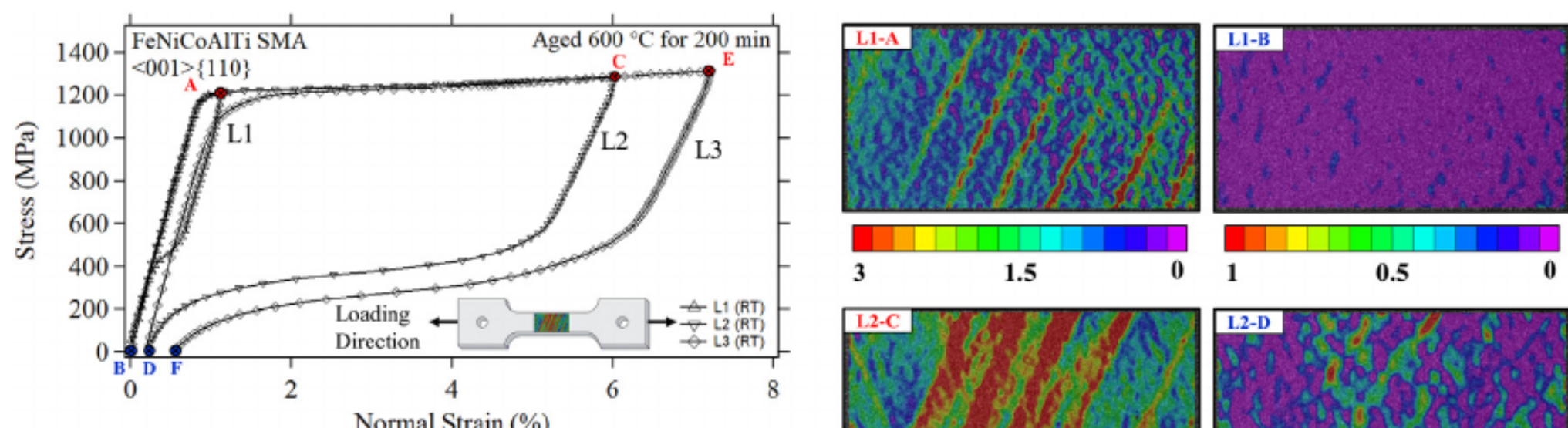


Fig. 6. (a) Incremental stress-strain curves of a single crystalline sample aged for 180 min at 600 °C. (b) The total recovery properties and residual accumulated strain (global) for each loading cycle reported in (a). (c) Full-field contour plots of the normal strains captured at the maximum stress for each loading cycle (L1–L4). (d) DIC strain contour plots of the residual strains at points B, D, F, and G marked in (a).

200 min aging times, both at 600 °C. Although both samples exhibited SE strains, the strength of the sample subjected to the 200 min treatment was, as expected, higher compared to the sample exposed to 180 min of aging only. It is easy to explain the increase in strength based on the higher volume fraction of precipitates which is expected for the slightly longer aging treatment. However, it remains unclear how the local response will be affected, in particular, the accumulation of local, and eventually global, residual strains with continued loading and at higher levels of imposed deformation. To shed further insight into the effects introduced by aging in the SE regime, two samples

with different aging conditions (*i.e.*, 180 min and 200 min) were incrementally loaded up to 7% global strain and unloaded. The incremental loading curves for the 180 min aged sample and 200 min sample are presented in Figs. 6 and 7, respectively. The evolution of residual strains and recovery levels for all the loading cycles (shown in Figs. 6b and 7b) do not point to any discernable difference between the considered aging conditions even though a wider hysteresis is observed for the longer aging time.

The full-field DIC contour plots shown in Figs. 6–7 were captured at the maximum stress and following unloading for each of the



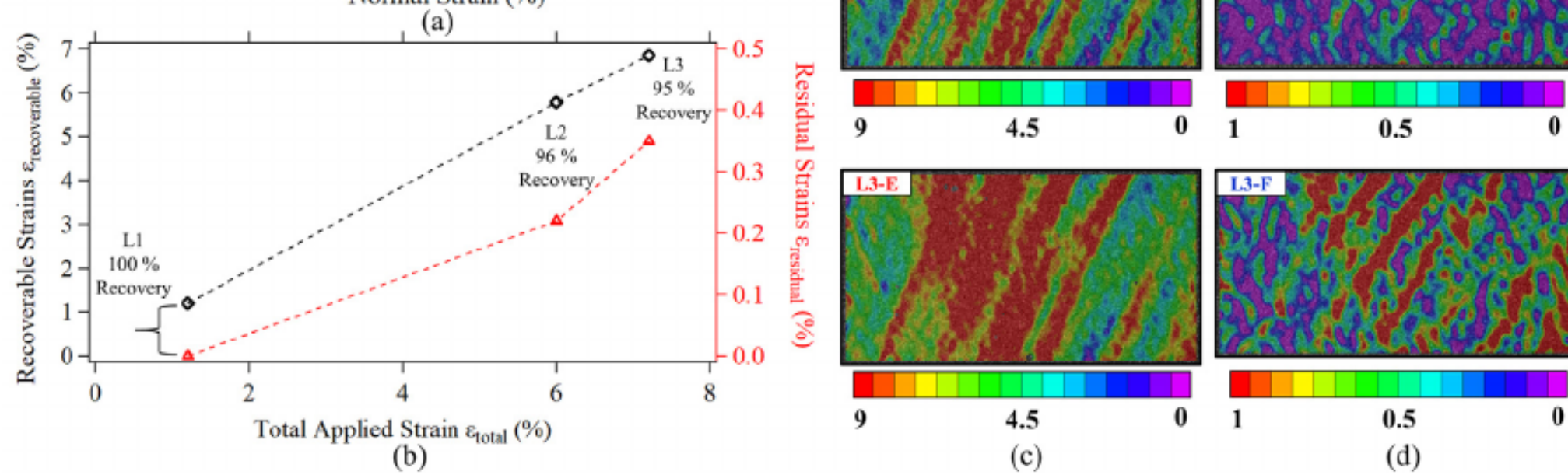


Fig. 7. (a) Incremental stress-strain curves of a single crystalline sample aged for 200 min at 600 °C. (b) The total recovery properties and residual accumulated strain (global) for each loading cycle reported in (a). (c) Full-field contour plots of the normal strains captured at the maximum stress for each loading cycle (L1–L3). (d) DIC strain contour plots of the residual strains at points B, D, and F marked in (a).

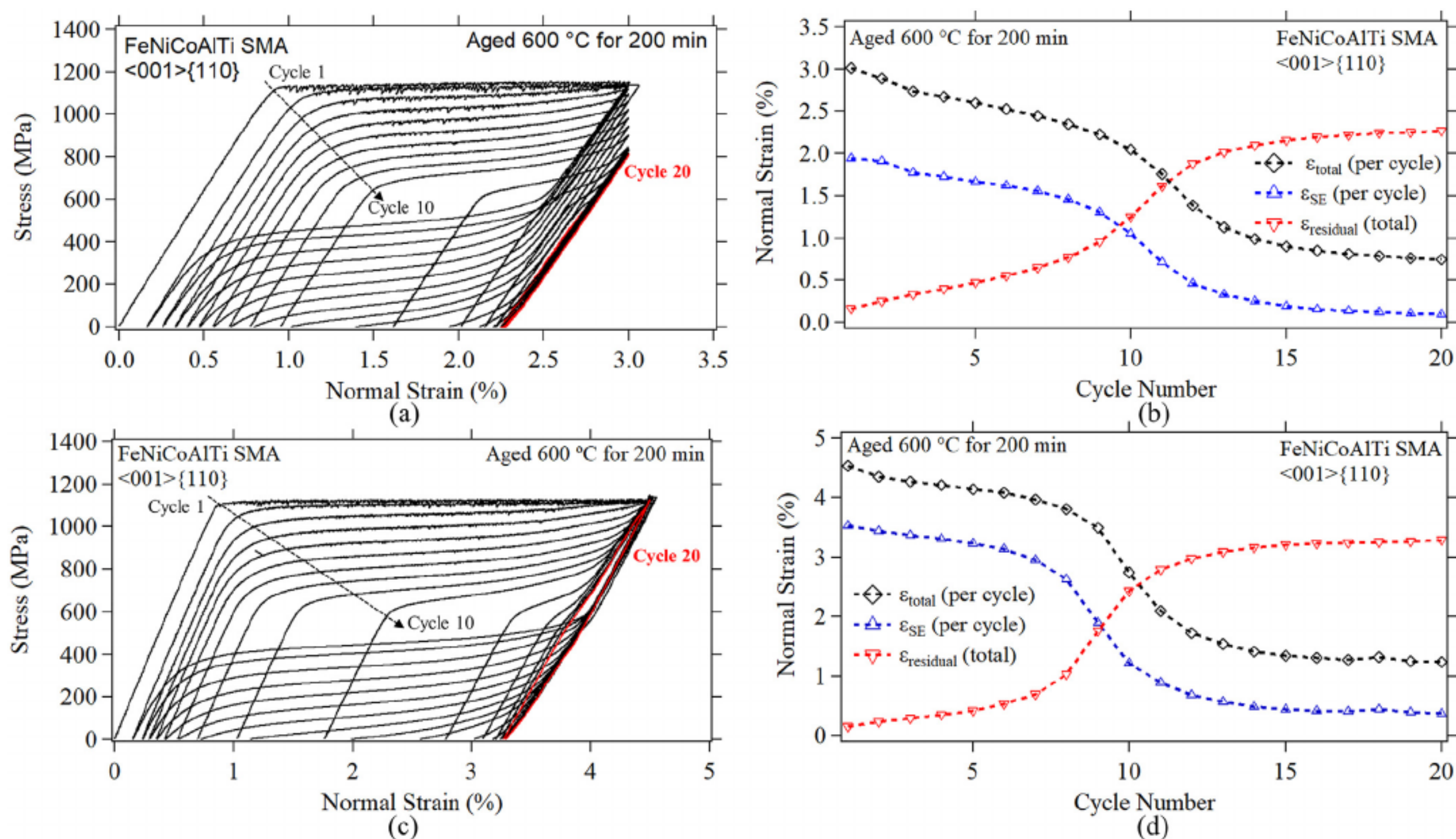


Fig. 8. (a) Cyclic stress-strain curves (3% applied strain) of a single crystalline sample aged for 200 min at 600 °C. (b) The evolution of the total average strain (), SE strain (), and residual strain () for the cyclic loading results shown in (a). (c) Cyclic stress-strain curves (4.5% applied strain) of a single crystalline sample aged for 200 min at 600 °C. (d) The evolution of the total average strain (), SE strain (), and residual strain () for the cyclic loading results shown in (c).

deformation cycles. It is noted that multiple martensite variants were activated in all cases and at all loading levels and that their volume fraction increased at higher applied strains. Despite the formation of multiple variants of martensite, the deformation fields were primarily dominated by only one as observed by intense strain band formation along one direction. Both samples shared this feature, however, the dominating martensite variant differed. The local variation in the stress field which is associated with different precipitation size and volume fraction may have contributed to such dissimilar behavior. The full-field contour plots captured at the unloaded states point to the magnitude, and location of residual strains. By comparing the DIC contour

plots with the corresponding results obtained at the maximum applied stresses, it is noted that the spatial locations for residual strain accumulation do not necessarily coincide with the locations of maximum applied strains. Further discussion of the implication of this observation is provided in Section 4.

The results presented thus far for the 180 min and 200 min aging treatments point to an insignificant difference in the macro-scale SE strains and average recovery properties. However, the critical transformation stress, stress hysteresis (Figs. 6a and 7a), and the local SE strains (*i.e.*, the dominating martensite variant) differed for the considered aging times. As one of the aims of this work is to better understand

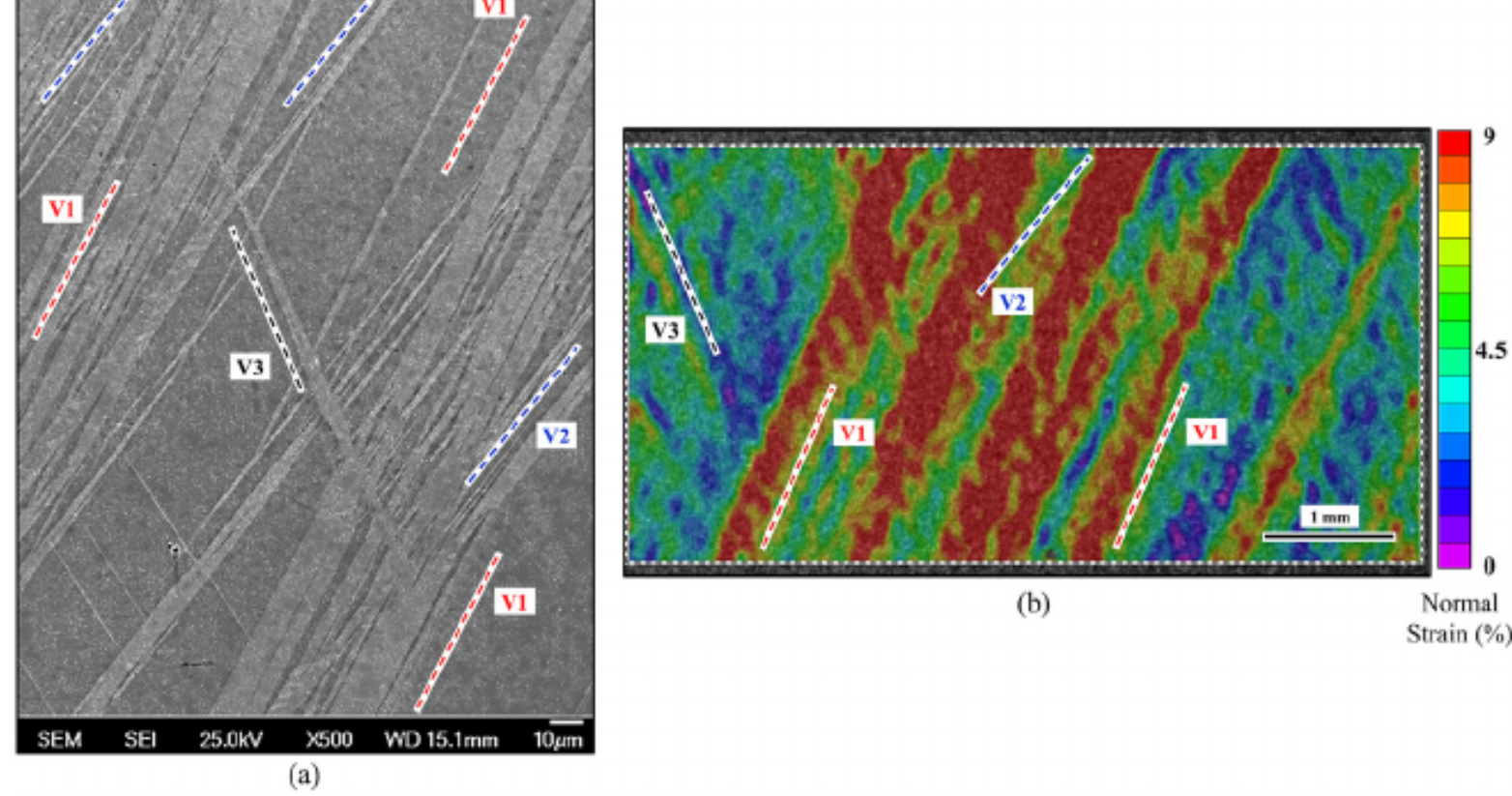


Fig. 9. (a) SEM micrograph revealing the accumulation of residual martensite following cyclic loading (see Fig. 8c for stress-strain curves). The marked martensite variants (V1–V3) match the localized strain bands induced during transformation as shown for a representative case in (b).

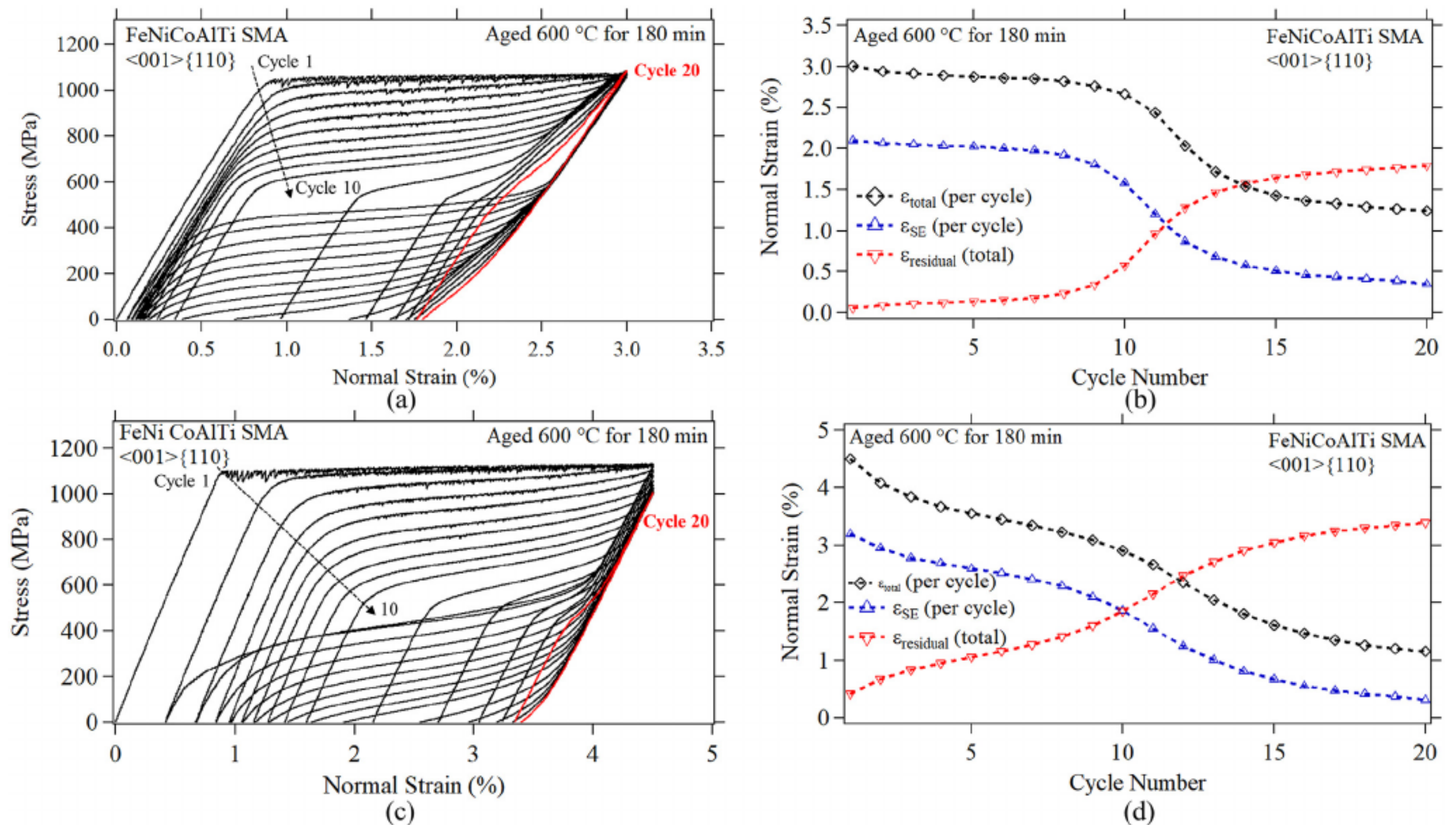
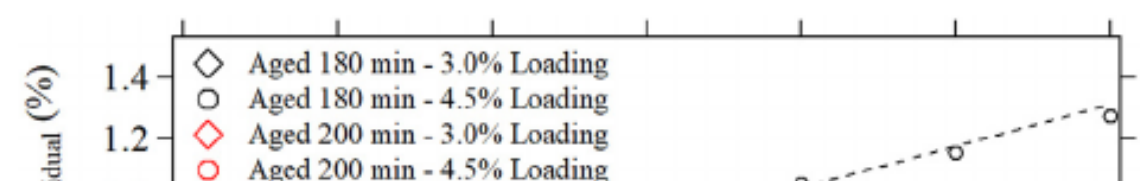


Fig. 10. (a) Cyclic stress-strain curves (3% applied strain) of a single crystalline sample aged for 180 min at 600 °C. (b) The evolution of the total average strain (), SE strain (), and residual strain () for the cyclic loading results shown in (a). (c) Cyclic stress-strain curves (4.5% applied strain) of a single crystalline sample aged for 180 min at 600 °C. (d) The evolution of the total average strain (), SE strain (), and residual strain () for the cyclic loading results shown in (c).

the functional fatigue properties of the Fe-based SMA under investigation, it is important to analyze the stability of the SE strains under cyclic loading conditions and how the different heat treatments affect the functional fatigue properties of this alloy at different levels of loading. Fig. 8a reports the cyclic stress-strain response for a FeNiCoAlTi sample subjected to a constant 3% applied average strain for 20 cycles. The evolution of the total average strain (), SE strain (), and residual strain () are shown in Fig. 8b. A clear degradation in the SE strains is observed in the first 10 cycles followed by a sharp drop and an accelerated rate of degradation in SE properties due to the buildup

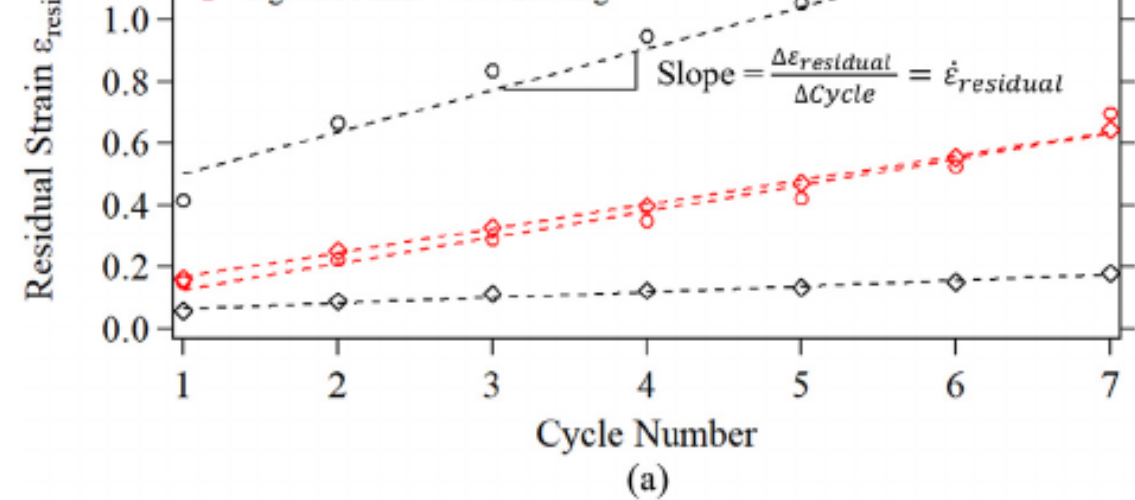
an accelerated buildup of residual strains. As pointed previously, local accumulation of residual strains takes place even with seemingly insignificant levels of average residual strains at the macro-scale (see Fig. 5). This incremental increase in local residual strains results in the later degradation in the macro-scale properties as shown in Fig. 10b. The evolution of the residual and SE strains exhibited similar trends to the



of residual strains. Similar trends were observed at higher levels of applied strain (i.e., 4.5%) as reported in Fig. 8c–d. However, the rate of accumulation of residual strains, and consequently the degradation in SE strains, varied slightly.

The clear degradation in the magnitude of SE strains (shown in Fig. 8) was induced by the incremental accumulation of residual strains during cyclic loading. The full-field strain measurements provide an accurate assessment of the level, and spatial location, of residual strain accumulation. However, the microstructural aspects associated with permanent shape change require further investigation. Fig. 9a shows an SEM micrograph of the fatigued sample's surface discussed in Fig. 8c. Following 20 cycles of cyclic loading at 4.5% applied strains, the SEM image reveals the accumulation of residual martensite. The observed variants (V1–V3 as marked in Fig. 8a) match the localized strain bands associated with martensite transformation (a representative DIC contour plot is shown in Fig. 8b). These observations highlight that the source of residual strain accumulation was the associated with the buildup of non-transforming residual martensite.

The cyclic stress-strain response for the FeNiCoAlTi samples aged for 180 min, which is the second aging treatment being considered for functional fatigue properties, is shown in Fig. 10. The sample subjected to 3% applied strain exhibited minimal accumulation residual strains initially, however, a transition took place around the 10th cycle with



Aging Heat Treatment	Loading Conditions Applied Strain ϵ (%)	$\dot{\epsilon}_{\text{residual}}$ (%/cycle)
600 °C – 180 min	3.0	0.018
600 °C – 180 min	4.5	0.134
600 °C – 200 min	3.0	0.078
600 °C – 200 min	4.5	0.084

Fig. 11. (a) Evolution of the residual strains for samples subjected to different aging treatments and loading conditions. (b) Comparison of the residual strain accumulation rate ($\dot{\epsilon}_{\text{residual}}$) for the results presented in (a).

results obtained from the 200 min aging times. However, the complete loss of superelastic properties, as shown by the essentially elastic stress-strain curves in Fig. 9a and c at cycle 20 (i.e., elastic shakedown), was not reached for the 180 min aged samples.

The evolution of residual strains and the associated degradation in superelastic strains under cyclic loading condition differed for the two aging conditions and loading levels discussed in Figs. 9–10. For a better quantitative evaluation, we focus on the first few cycles prior to the inflection and sharp spike in residual strain which was observed around the 10th fatigue cycle. Fig. 11 shows a comparison between the measured macro-scale residual strains for the 180 min and 200 min aging treatments, both with two cyclic loading levels 3% and 4.5%. A summary of the residual strain accumulation rate, $\dot{\epsilon}_{\text{residual}}$, which is defined using the slope as shown in Fig. 11a, is presented in Fig. 11b. The strain accumulation rate for both aging treatments experienced an increase at 4.5% loading level compared to 3%. However, it is noted that the sample aged for 180 min and subjected to 3% cyclic strain experienced a significantly lower accumulation rate compared to all other samples.

4. Discussion

The development and optimization of Fe-based shape memory alloys has a great potential to provide cost-effective alternatives to NiTi, thus allowing a wider range of applications utilizing their unique shape memory and superelastic properties. The results presented in this paper illustrate considerable promise of FeNiCoAlTi alloys, one of the Fe-based SMA compositions currently being explored, to achieve superelasticity upon optimization of aging heat treatment. In addition, the work provides a deep insight into the functional fatigue response of this class of alloys when subjected to cyclic loading. In particular, the notion of plastic flow limiting functionality is explored further with cyclic tests showing dramatic reduction of superelastic strains upon accumulation of irrecoverable plastic strains.

The results presented in this work fit the pattern of Fe-based SMAs being limited by plastic flow. Previously there were two problems with iron-based SMAs. The first has been the very large stress hysteresis (FeNiCoTi and FeMnSi) which precludes the occurrence of superelasticity. The second is the role of plastic deformation curtailing

a challenge for FeNiCoAlTi SMAs. Under cyclic loading conditions, significant degradation in SE strains took place, particularly beyond the 10th loading cycle as shown in Fig. 8. The low levels of irrecoverable strains at the commencement of loading (i.e., cycles 1–10) underestimate the local accumulation of residual strains. The results presented in Fig. 5 clearly highlight SE behavior with insignificant residual strains based on typical global measurements. However, the full-field and local strain measurements point to a finite accumulation of irrecoverable strains, locally. The gradual buildup of these local strains eventually results in measurable accumulation, globally, and loss of functionality with continued loading. Plastic flow certainly plays a significant role in this process due to the large transformation shear (misfit strains) that occur at interfaces and the accumulation of dislocations which act to pin the martensite phase boundary and prevent reverse transformation, thus resulting in the gradual buildup of residual martensite (see SEM micrograph in Fig. 9a). In addition, the activation of multiple martensite variants, and their interaction, also affects the local plastic strain accumulation resulting in further degradation of SE properties.

The rate of irrecoverable plastic strain accumulation varies, as expected, with the magnitude of imposed cyclic strain. The aging treatment and the resulting precipitation content is also a contributing factor affecting the functional fatigue response as shown in Figs. 8 and 10. The formation of residual martensite in the vicinity of nano-precipitates has been reported to degrade the cyclic stability of FeNiCoAlTa SMA [16]. A similar impact for the γ' precipitates is expected in the case of FeNiCoAlTi SMA considered in this work. However, despite having an impact on the total SE strain degradation, the first order effects is still expected to be related to plasticity at the martensite-austenite interface and due to the formation of intersecting multiple variants of martensite. The fact that plastic strain accumulation rates under different loading conditions and different aging treatments, and thus precipitation, were similar in the first few cycles (Fig. 11b) supports this conclusion.

5. Conclusions

The work supports the following conclusions:

1- FeNiCoAlTi single crystalline samples loaded along the $\langle 001 \rangle$ direc-

the shape memory effect. With the introduction of Al as an alloying element and the process of precipitation, the current alloy has overcome the superelasticity limitation of earlier alloys. It has been well documented that the presence of these non-transforming nano-precipitates promotes reversible martensitic transformation by increasing the critical stress for slip [19,27,31,39]. However, as reported and discussed in the current work, the forward martensite transformation stress is also altered and increased but at a different rate compared to slip resistance. A proper optimization and control of the precipitation process, through aging treatments, is crucial to introduce sufficient increase in slip resistance with acceptable levels of transformation stresses. Introducing this gap between these two stress levels (with the transformation stress being lower than the critical slip stress) is conducive to martensitic transformation and superelasticity. Recent studies have focused on assessment of slip resistance in shape memory alloys [13]. It was demonstrated that slip resistance is stress-state and crystal orientation dependent and need to significantly exceed the transformation stress levels for full superelasticity and shape memory to be realized. In the case of FeNiCoAlTi alloy investigated in this work, despite being able to achieve transformation stresses that are lower than slip levels, achieving a significant gap between the two stresses was challenging through precipitation (*i.e.*, requires longer aging times to widen the gap between slip and transformation stresses) and was eventually limited by brittle behavior at longer aging times or higher aging temperatures.

Despite exhibiting the desirable room temperature superelasticity with recoverable strains of up to ~8%, the functional behavior remains

tion exhibit superelastic response at RT following precipitation heat treatment. In the absence of such heat treatment, slip mediated plasticity commences at relatively low stress levels that are less than the critical martensitic transformation stress.

- 2- A proper optimization and control of the precipitation process, through aging treatments, is crucial to introduce sufficient increase in slip resistance with acceptable levels of transformation stresses. Introducing this gap between these two stress levels is conducive to martensitic transformation and superelasticity.
- 3- Samples optimized for RT superelasticity exhibited similar deformation response at lower temperatures, down to ~ 100 °C, at which incomplete recovery was observed. The M_s was determined to be around 100 °C for this alloy, given the selected heat treatment, which would explain the degradation in SE properties once deformation was conducted at this temperature.
- 4- Good superelastic properties with large recoverable strains (~7% recoverable strains) and high recovery levels (>95% recovery) were obtained from global measurements of deformation. Local measures, however, pointed to finite accumulation of residual strains which were not detectable (initially) using global and averaged measures of strain.
- 5- Under cyclic loading conditions, limited degradation of SE properties took place in the first 10 cycles of loading. However, significant degradation took place with continued loading. The loss of functionality was attributed to the gradual buildup of local irrecoverable strains. A process that has been induced by plasticity at the martensite-

austenite boundary which acts to pin the interface and prevent reverse transformation.

Data availability

The data discussed in this study will be made available upon request.

Author contributions section

Both authors contributed to the preparation of the manuscript.

Acknowledgements

The work is supported by a National Science Foundation grant NSF DMR 1709515 and partially by NSF CMMI - 1333884 which is gratefully acknowledged. The authors acknowledge the assistance of Prof. Yury Chumlyakov (Tomsk State University) with preparation of single crystals. The corresponding author would like to acknowledge the partial financial support from the Materials Science and Engineering Research Institute at the American University of Sharjah.

References

- [1] J. Mohd Jani, M. Leary, A. Subic, M.A. Gibson, A review of shape memory alloy research, applications and opportunities, *Mater. Des.* (1980–2015) 56 (2014) 1078–1113.
- [2] W. Huang, On the selection of shape memory alloys for actuators, *Mater. Des.* 23 (1) (2002) 11–19.
- [3] D.C. Lagoudas, *Shape Memory Alloys: Modeling and Engineering Applications*, Springer, New York, 2008.
- [4] C. Lexcellent, *Shape-memory Alloys Handbook* (ISTE; ISTE.), Wiley, Hoboken, 2013.
- [5] C. Nares, P.S.C. Bose, C.S.P. Rao, Shape memory alloys: a state of art review, *IOP Conf. Ser. Mater. Sci. Eng.* 149 (1) (2016) 012054.
- [6] B. O'Brien, F.M. Weafer, M.S. Bruzzi, 1.3 Shape memory alloys for use in medicine A2 - Ducheyne, Paul, *Comprehensive Biomaterials II*, Elsevier, Oxford 2017, pp. 50–78.
- [7] H. Sehitoglu, L. Patriarca, Y. Wu, Shape memory strains and temperatures in the extreme, *Curr. Opin. Solid State Mater. Sci.* 21 (2016) 113–120.
- [8] *Shape Memory Materials* (Shape Memory Materials)., Cambridge University Press, 1999 284.
- [9] S. Takaoka, 6 - Overview of the development of shape memory and superelastic
- [16] P. Krooß, et al., Cyclic degradation mechanisms in aged FeNiCoAlTa shape memory single crystals, *Acta Mater.* 79 (2014) 126–137.
- [17] T. Maruyama, H. Kubo, 12 - Ferrous (Fe-based) shape memory alloys (SMAs): properties, processing and applications, *Shape Memory and Superelastic Alloys*, Woodhead Publishing 2011, pp. 141–159.
- [18] J. Ma, B. Kockar, A. Evirgen, I. Karaman, Z.P. Luo, Y.I. Chumlyakov, Shape memory behavior and tension–compression asymmetry of a FeNiCoAlTa single-crystalline shape memory alloy, *Acta Mater.* 60 (5) (2012) 2186–2195.
- [19] Y. Tanaka, R. Kainuma, T. Omori, K. Ishida, Alloy design for Fe-Ni-Co-Al-based superelastic alloys, *Mater. Today Proc.* 2 (2015) S485–S492.
- [20] L.W. Tseng, J. Ma, S.J. Wang, I. Karaman, Y.I. Chumlyakov, Effects of crystallographic orientation on the superelastic response of FeMnAlNi single crystals, *Scr. Mater.* 116 (2016) 147–151.
- [21] Y. Tanaka, Y. Himuro, R. Kainuma, Y. Sutou, T. Omori, K. Ishida, Ferrous polycrystalline shape-memory alloy showing huge superelasticity, *Science* 327 (5972) (2010) 1488–1490.
- [22] T. Omori, et al., Superelastic effect in polycrystalline ferrous alloys, *Science* 333 (6038) (2011) 68.
- [23] M. Vollmer, et al., Cyclic degradation in bamboo-like Fe–Mn–Al–Ni shape memory alloys – the role of grain orientation, *Scr. Mater.* 114 (2016) 156–160.
- [24] J. Ma, B.C. Hornbuckle, I. Karaman, G.B. Thompson, Z.P. Luo, Y.I. Chumlyakov, The effect of nanoprecipitates on the superelastic properties of FeNiCoAlTa shape memory alloy single crystals, *Acta Mater.* 61 (9) (2013) 3445–3455.
- [25] L.W. Tseng, J. Ma, I. Karaman, S.J. Wang, Y.I. Chumlyakov, Superelastic response of the FeNiCoAlTi single crystals under tension and compression, *Scr. Mater.* 101 (2015) 1–4.
- [26] H. Sehitoglu, I. Karaman, X.Y. Zhang, Y. Chumlyakov, H.J. Maier, Deformation of FeNiCoTi shape memory single crystals, *Scr. Mater.* 44 (5) (2001) 779–784.
- [27] P. La Roca, A. Baruj, C.E. Sobrero, J.A. Malarria, M. Sade, Nanoprecipitation effects on phase stability of Fe-Mn-Al-Ni alloys, *J. Alloys Compd.* 708 (2017) 422–427.
- [28] H. Ozcan, et al., Effects of cyclic heat treatment and aging on superelasticity in oligocrystalline Fe-Mn-Al-Ni shape memory alloy wires, *Scr. Mater.* 134 (2017) 66–70.
- [29] Y.I. Chumlyakov, I.V. Kireeva, V.V. Poklonov, Z.V. Pobedennaya, I. Karaman, The shape-memory effect and superelasticity in single-crystal ferromagnetic alloy FeNiCoAlTi, *Tech. Phys. Lett.* 40 (9) (2014) 747–750.
- [30] Z.V. Pobedennaya, K.A. Reunova, I.V. Kireeva, Y.I. Chumlyakov, Shape memory effect and superelasticity in single crystals of iron-based alloys, *IOP Conf. Ser. Mater. Sci. Eng.* 93 (1) (2015) 012044.
- [31] Y.I. Chumlyakov, et al., Thermoelastic martensitic transformations in single crystals of FeNiCoAlX(B) alloys, *Russ. Phys. J.* 58 (11) (March 01 2016) 1549–1556.
- [32] P. Chowdhury, H. Sehitoglu, Deformation physics of shape memory alloys – fundamentals at atomistic frontier, *Prog. Mater. Sci.* 88 (2017) 49–88.
- [33] Y. Geng, et al., Coherency of ordered γ' precipitates and thermoelastic martensitic transformation in FeNiCoAlTaB alloys, *J. Alloys Compd.* 628 (2015) 287–292.
- [34] O.A. Kuts, M.Y. Panchenko, I.V. Kireeva, Y.I. Chumlyakov, Shape memory effect and superelasticity in [001] single crystals of FeNiCoAlNb(B) alloys, *IOP Conf. Ser. Mater. Sci. Eng.* 93 (1) (2015) 012034.

- alloy applications, Shape Memory and Superelastic Alloys, Woodhead Publishing 2011, pp. 77–84.
- [10] S. Barbarino, E.I.S. Flores, R.M. Ajaj, I. Dayyani, M.I. Friswell, A review on shape memory alloys with applications to morphing aircraft, *Smart Mater. Struct.* 23 (6) (2014) 063001.
- [11] M.H. Elahinia, M. Hashemi, M. Tabesh, S.B. Bhaduri, Manufacturing and processing of NiTi implants: a review, *Prog. Mater. Sci.* 57 (5) (2012) 911–946.
- [12] G. Eggeler, E. Hornbogen, A. Yawny, A. Heckmann, M. Wagner, Structural and functional fatigue of NiTi shape memory alloys, *Mater. Sci. Eng. A* 378 (1) (2004) 24–33.
- [13] H. Sehitoglu, S. Alkan, Recent progress on modeling slip deformation in shape memory alloys, *Shape Mem. Superelasticity* 4 (1) (March 01 2018) 11–25.
- [14] S. Saadat, et al., An overview of vibration and seismic applications of NiTi shape memory alloy, *Smart Mater. Struct.* 11 (2) (2002) 218.
- [15] A. Cladera, B. Weber, C. Leinenbach, C. Czaderski, M. Shahverdi, M. Motavalli, Iron-based shape memory alloys for civil engineering structures: an overview, *Constr. Build. Mater.* 63 (2014) 281–293.
- [35] Z.V. Pobedennaya, K.A. Reunova, I.V. Kireeva, Y.I. Chumlyakov, Shape memory effect and superelasticity in single crystals of iron-based alloys, *IOP Conf. Ser. Mater. Sci. Eng.* 93 (1) (2015) 012044.
- [36] D. Roy, V. Buravalla, P.D. Mangalgi, S. Allegavi, U. Ramamurty, Mechanical characterization of NiTi SMA wires using a dynamic mechanical analyzer, *Mater. Sci. Eng. A* 494 (1) (2008) 429–435.
- [37] Y. Liu, J. van Humbeeck, On the damping behaviour of Niti shape memory alloy, *J. Phys. IV France* 07 (1997) C5 (C5-519-C5-524).
- [38] A. Fabregat-Sanjuan, F. Gispert-Guirado, F. Ferrando, S. De la Flor, Identifying the effects of heat treatment temperatures on the Ti₅₀Ni₄₅Cu₅ alloy using dynamic mechanical analysis combined with microstructural analysis, *Mater. Sci. Eng. A* 712 (2018) 281–291.
- [39] C. Zhang, et al., Understanding phase stability of Al-Co-Cr-Fe-Ni high entropy alloys, *Mater. Des.* 109 (Supplement C) (2016) 425–433.